Nanoscale

PAPER

View Article Online
View Journal | View Issue

Cite this: *Nanoscale*, 2025, **17**, 24715

Tailored photoactivity of 2D nanosheets synthesized by electron irradiation of metal–organic Ru(II) monolayers

Maria Küllmer,[a] Alexander K. Mengele,[b] Julian Kund,[c] Robert Leiter,[d] Felix Herrmann-Westendorf,[a,e] Daniel Hüger,[a] Rebecka Gläßner,[a] Emad Najafidehaghani,[a] Hamid Reza Rasouli,[a] Christof Neumann,[a] Johannes Biskupek,[d] Lara S. Dröge,[a] Verena Müller,[a] Kamil Witas,[b] Martin Presselt,[e] Thomas Weimann,[f] Benjamin Dietzek-Ivanšić,[a,e,g,h,i] Ute Kaiser,[d] Christine Kranz,[c] Sven Rau[b] and Andrey Turchanin*[a,g,h]

Received 26th June 2025,
Accepted 30th September 2025

DOI: 10.1039/d5nr02717a

rsc.li/nanoscale

Two-dimensional materials gain significant interest for applications in light harvesting and sensing due to their unique properties and low dimensions. A key challenge is the introduction of specific functionalities such as photoactivity as well as their adjustment. Using adaptable coordination compounds as building blocks for 2D nanosheets offers a promising approach for the controlled optimization of these functionalities. In this study, we demonstrate the preparation of carbonaceous 2D materials by self-assembling thiolated Ru(II) polypyridine complexes (RuSH) onto gold surfaces, followed by electron beam-induced crosslinking into nanosheets. The modular design of the complexes enables the variation of substituents on the bipyridine ligands, thereby influencing the nanosheets' mechanical stability and photoactivity. Spectroscopic analysis confirms that both the Ru(II) core and thiol group remain mostly intact during crosslinking, facilitating a future post-functionalization for catalysis applications. The resulting nanosheets, with areas up to cm^2 and thicknesses below 1 nm, exhibit outstanding electrochemical and optoelectrical activity, making them promising candidates for catalysis, sensing, and miniaturized devices.

1. Introduction

The efficient utilization of sunlight is considered as a key solution to overcome the limitations and environmental disadvantages of fossil energy sources in *e.g.* transport or industry.[1–3] In that respect, a variety of materials and systems have been developed so far which convert light into electrical energy and/or catalyze the generation of H_2.[4,5] Among these concepts, 2D materials as well as single molecule catalysts are found, each offering unique advantages. The 2D materials thickness of only a few atoms implies that all active centers are easily accessible for catalysis.[6–8] Single molecule catalysts and photosensitizers offer enormous variability as small changes of the molecular structure strongly influence the molecules photophysical properties and redox behavior.[5] The advantages of both material classes are combined by constructing nanosheets from small, functional molecules as photoactive units. By adjusting the molecules' structure selectively, the properties of the 2D material can be tailored to match the specific needs of the application.[9–12] In addition, the stability and catalytic performance of such molecular catalysts and photosensitizers can be improved due to matrix incorporation.[5,13–15] Low-energy electron beam irradiation of self-assembled monolayers (SAMs) lithographically generates single sheet 2D materials called carbon nanomembranes (CNMs).[16–18] These nanometer-thin membranes have large lateral dimensions in the cm^2 range, while their chemical stability is comparable to that of graphene.[16–19] The choice of the molecular precursor deter-

---

[a] *Institute of Physical Chemistry, Friedrich Schiller University Jena, Lessingstraße 10, 07743 Jena, Germany. E-mail: andrey.turchanin@uni-jena.de*
[b] *Institute of Inorganic Chemistry I, Ulm University, Albert-Einstein-Allee 11, 89081 Ulm, Germany*
[c] *Institute of Analytical and Bioanalytical Chemistry, Ulm University, Albert-Einstein-Allee 11, 89081 Ulm, Germany*
[d] *Electron Microscopy Group of Materials Science, Ulm University, Albert-Einstein-Allee 11, 89081 Ulm, Germany*
[e] *Leibniz Institute of Photonic Technology e. V. (IPHT), Albert-Einstein-Straße 9, 07745 Jena, Germany*
[f] *Physikalisch-Technische Bundesanstalt (PTB), Bundesallee 100, 38116 Braunschweig, Germany*
[g] *Jena Center for Soft Matter (JCSM), Friedrich Schiller University Jena, Philosophenweg 7, 07743 Jena, Germany*
[h] *Center for Energy and Environmental Chemistry Jena (CEEC Jena), Philosophenweg 7a, 07743 Jena, Germany*
[i] *Leibniz Institute of Surface Engineering, Permoserstraße 15, 04318 Leipzig, Germany*

mines the function and thickness of the final CNM.[19,20] CNMs made from self-assembled terpyridine biphenyl thiols turned, *e.g.*, luminescent due to binding of lanthanide ions.[21] Another example of our previous work is the CNM made from carboxylated Ru(II) complexes with a thickness of ~3 nm, which repeatably shows photoactivity upon periodic illumination with visible light.[22] The impact of the electron-beam irradiation on the precursors molecular structures needs to be assessed as bond cleavage and crosslinking[23–27] can influence the nanosheets' functionality. The following work demonstrates the promotion of intrinsic photoactivity in nanosheets with thicknesses <1 nm through optimization of the precursor structures, thiolated Ru(II) polypyridine complexes (RuSH) with varying distal substituents. Methods from molecular synthesis and material characterization are combined to relate the precursors' properties to those of the created nanosheets.

Fig. 1 shows the modular synthesis of the Ru(II) polypyridine precursors $[(bpy)_2Ru(phen(SBn)_2)](PF_6)_2$ **1**, $[(dmbpy)_2Ru(phen(SBn)_2)](PF_6)_2$ **2**, and $[(tbbpy)_2Ru(phen(SBn)_2)](PF_6)_2$ **3**.[28] The complexes are characterized by nuclear magnetic resonance (NMR), high-resolution mass spectrometry (HRMS), UV-Vis absorption spectroscopy, emission and emission excitation spectroscopy. These precursors are then activated by deprotection cleaving the S-benzyl bond to form thiolate functions which allow self-assembly into monolayers on Au substrates forming the RuSH SAMs **4**, **5**, and **6**, respectively. Lastly, irradiation *via* low-energy electron beam converts the SAMs into the nanosheets RuSH CNM **7**, **8** and **9**. Self-assembly and the nanosheet formation are characterized by X-ray photoelectron spectroscopy (XPS) and atomic force microscopy (AFM). The stability of the freestanding nanosheets as well as the influence of the substituents on the stability is assessed by scanning electron microscopy (SEM). With scanning and atomically resolved high-resolution transmission electron microscopy (STEM, HRTEM) as well as energy dispersive X-ray spectroscopy (EDX) information on the distribution of photoactive centers and the atomic nanosheet structure are obtained. The retention of the molecular building blocks' spectroscopical properties is characterized by photothermal deflection spectroscopy (PDS) and Raman scattering. Square wave voltammetry (SWV) and cyclic voltammetry (CV) as well as optoelectrical measurements reveal the nanosheets' electrochemical properties and photoactivity. Finally, the optical and electrochemical activity of the nanosheets is evaluated with respect to the luminescence quenching of the molecular Ru(II) polypyridines complexes which are the building blocks of this nanostructure. As luminescence capability of metal complexes is strongly influenced by changes of the ligand structures, this investigation represents a powerful tool for not only assessing the material properties but also to answer the question on whether the building block has retained its property during the electron beam induced polymerization process. In this way, changes in nanosheet photoactivity can be linked to variations in precursor structure.

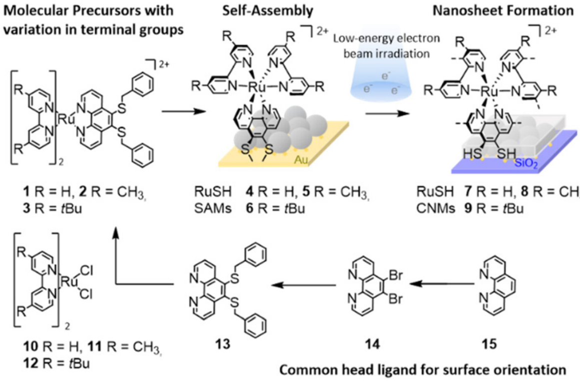

Fig. 1 Preparation of RuSH CNMs **7–9** by self-assembly of Ru(II) precursors **1**, **2** or **3** into the respective SAMs **4–6** and subsequent low-energy electron beam irradiation. Terminal groups of the complexes can be varied due to the modularity of the precursors **10**, **11** and **12**. The thiolated phenanthroline **13** serves as a common head group and enforces the attachment of the phenanthroline ligand on the Au surface.

2. Experimental section

2.1 Sample preparation

The synthesis of the molecular precursors **1**, **2** and **3** as well as their detailed characterization including NMR, HRMS, UV-Vis absorption spectroscopy, emission and emission excitation spectroscopy can be found in the SI section 1. $Phen(SBn)_2$ **13** was synthesized by bromination of 1,10-phenanthroline **15** followed by a nucleophilic aromatic substitution of the resulting 5,6-dibromo-1,10-phenanthroline **14** with *in situ* prepared sodium benzylthiolate.[29] Preparation of $[(bpy)_2RuCl_2]$ **10**, $[(dmbpy)_2RuCl_2]$ **11** and $[(tbbpy)_2RuCl_2]$ **12** was conducted according to literature procedures.[30] The microwave assisted ligand exchange reaction of **10**, **11** or **12** with the thiolated head ligand **13** followed by precipitation with NH_4PF_6 yielded the molecular precursors **1**, **2** and **3** employed for self-assembly on gold. Conditions for self-assembly of **1**, **2** and **3** on Au under N_2 atmosphere are described in detail in section 2 of the SI. In summary, the precursors **1**, **2** and **3** were deprotected with $AlCl_3$ in CH_2Cl_2 shortly before self-assembly to release the thiols. After solvent removal and filtration the residue was dissolved in *N*,*N*-dimethylformamide (DMF). 300 nm Au(111) films on mica were immersed in these solutions for typically 48 h under N_2 atmosphere at room temperature to yield finally the SAMs **4**, **5** and **6**.

Cross-linking of the Ru(II) SAMs into the CNMs **7**, **8** and **9** was performed either in a high vacuum chamber equipped with an electron gun (FG15/40, Specs) at a base pressure of $<5 \times 10^{-8}$ mbar or in the Multiprobe System used as well for XPS measurements (Scienta Omicron) under ultra-high vacuum (base pressure 2×10^{-10} mbar, electron gun NEK-150-SC, Staib). In both cases the SAMs were irradiated with an electron beam with a kinetic energy of 50 eV and a dose of 50 mC cm^{-2}. The so formed CNMs can be placed on various substrates as required by the specific characterization method *via* a previously reported transfer procedure.[31] Details can be found as well in section 2 of the SI.

2.2 Nuclear magnetic resonance (NMR)

^{1}H (400 MHz or 500 MHz) and ^{13}C-NMR (101 MHz) spectra were recorded on Bruker Avance spectrometers at room temperature. The shift values are given in ppm and are referenced to the corresponding solvent residual peaks (7.26 ppm (singlet, ^{1}H-spectra) or 77.16 ppm (triplet, ^{13}C-spectra) for $CDCl_3$, 1.94 ppm (quintet, ^{1}H-spectra) or 118.26 ppm (singlet, ^{13}C-spectra) for CD_3CN).

2.3 High resolution mass spectrometry (HRMS)

HRMS was performed using a Fourier Transform Ion Cyclotron Resonance (FT-ICR) mass spectrometer solariX (Bruker Daltonics) equipped with a 7.0 T superconducting magnet and interfaced to an Apollo II Dual ESI/MALDI source. For all measurements *trans*-2-[3-(4-*tert*-butylphenyl)-2-methyl-2-propenylidene]malononitrile (DCTB) was used as matrix. Spectra were analyzed with the DataAnalysisViewer 4.2 from Bruker and transferred to Origin 9.0. Spectra simulation was performed with mMass Version 5.5.0 and transferred to Origin 9.0 as well.

2.4 X-ray photoelectron spectroscopy (XPS)

XPS characterization of SAMs and CNMs was conducted in an ultra-high vacuum (UHV) Multiprobe System (Scienta Omicron) with a base pressure of $<2 \times 10^{-10}$ mbar using an electron detector (Argus CU) with an energy resolution of 0.6 eV and a monochromatic Al K_α X-ray source under a photoelectron emission angle θ of 19° respective to the surface normal. CasaXPS was employed for XP spectra analysis. All spectra were calibrated to the substrates Au $4f_{7/2}$ peak at the binding energy (BE) of 84.0 eV. A linear (F 1s, N 1s, Cl 2p, S 2p) or Shirley (O 1s, C 1s, Au 4f) background was subtracted and components were fitted applying Voigt functions. The thicknesses of the SAMs and CNMs on gold were estimated by comparing their attenuated Au $4f_{7/2}$ signal to the signal of a freshly Ar^+ sputter-cleaned (FDG150 Focus) gold reference. Here, Beer–Lambert law for attenuation of the underlying Au $4f_{7/2}$ substrate signal was applied using an inelastic mean free path of λ_{IMFP} = 36 Å. As the Ru $3d_{3/2}$ peak is covered by the C 1s species, the Ru 3d doublet was fitted with a BE distance between Ru $3d_{5/2}$ and $3d_{3/2}$ of 4.2 eV, an intensity ratio of 3 : 2 and the same fwhm. The S2p doublets were fitted with a BE distance of 1.2 eV, the same fwhm and an intensity ratio of 2 : 1. Elemental ratios of XPS species were determined by using the Scofield relative sensitivity factors of the respective elements. For angle-resolved XPS (ARXPS), the spectra were acquired at θ = 0–80° with an angle step size of 10° or 20°. As shown before,[22,32] the relative intensities of the XP signals are obtained as a function of the peak areas of the elements recorded at θ normalized with the peak areas of the respective elements at θ = 0° and the Au $4f_{7/2}$ peak areas at θ and θ = 0°.

2.5 Atomic force microscopy (AFM) and scanning electron microscopy (SEM)

The SAMs and CNMs were characterized using a Ntegra AFM (NT MDT) in semi contact mode. The n-doped silicon AFM tips (NT-MDT) had resonance frequencies of 87–230 kHz and a tip radius of <10 nm. Freestanding CNMs on TEM grids were characterized with a Sigma VP (Carl Zeiss) SEM with the in-lens detector at a beam energy of 10–15 kV.

2.6 Scanning transmission electron microscopy (STEM) and high-resolution TEM (HRTEM)

(S)TEM data were obtained using a ThermoFisher Talos F200X TEM at an acceleration voltage of 120 kV. High-angle annular dark field (HAADF) and bright field (BF) signals as well as energy dispersive X-ray (EDX) spectra using a SuperX G2 detector were simultaneously acquired. Quantitative elemental maps were extracted from the EDX data using the ThermoFisher Velox software. Atomically resolved HRTEM images were recorded using the chromatic (C_C) and spherical aberration (C_S) corrected SALVE (Sub-Ångström Low Voltage Electron) microscope operated at 80 kV.

2.7 Surface-enhanced resonance Raman spectroscopy (SERRS)

SERRS was performed with a commercially available Raman microscope (WITec alpha 300 SR, WITec GmbH, Ulm, Germany) and a 488 nm laser as light source. The laser was focused on the sample employing a 100× microscope objective (NA 0.9), which is also used to collect the backscattered Raman light. To enhance photo stability during the measurements the power was reduced to 1 μW, leaving only minor degradation during the scans. Ag-nanoparticles were drop casted and dried on the SAMs and CNMs on Au prior SERRS measurements. The preparation of the Ag-nanoparticles is described in ref. 33. Since the obtained spectra were quite noisy, a Savitzky–Golay filter was applied.

2.8 Optical microscopy

Optical microscopy images were obtained with an Axio Imager Z1.m microscope (Carl Zeiss) and a thermoelectrically cooled 3-megapixel CCD camera (Axiocam 503 color, bright field operation).

2.9 UV-Vis absorption, emission and emission excitation spectroscopy

UV-Vis absorption spectroscopy was performed on a JASCO V-670 UV-vis-NIR Spectrophotometer using gas-tight quartz glass cuvettes (d = 10.0 mm, Hellma). Emission spectroscopy was performed on a JASCO FP-8500 Fluorescence Spectrometer with gas-tight quartz glass cuvettes (d = 10.0 mm, Hellma). Emission excitation spectra were recorded at the wavelength of maximum emission intensity of the respective complex (excitation wavelengths ranged from 250 to 600 nm) and compared to the ground state UV-Vis absorption spectrum by normalizing to the maximum of the metal-to-ligand charge transfer (MLCT) band.

2.10 Photothermal deflection spectroscopy

PDS was conducted on a setup described before.[22,34,35] Monochromatic light (1000 W Xe-high pressure lamp, 260 mm monochromator by LOT-QD) is modulated by a chopper

(Thorlabs) and focused on the sample. For measurement quartz pieces with monolayers of the CNMs **7**, **8**, **9** or an 8-layer stack of [1,1′-biphenyl]-4-thiol (BPT) were immersed into the solvent Fluorinert™ FC-770 (3 M™). The thermal lens created upon light absorption is then measured by the deflection of a HeNe-laser (0.5 mW) using a lateral effect sensor (PDA90, Thorlabs) as well as a lock-in amplifier (SRS-830, Stanford research systems). A 5 × 30 mm^2 glassy carbon sample was used as reference.

2.11 Optoelectrical experiments

Optoelectrical experiments were conducted using a 520 nm laser (LP520-SF15 model, Thorlabs) at various laser powers of 3.2, 43.5, and 89.6 mW cm^{-2}. The microfabrication of graphene field-effect transistor (GFET) chips is described in ref. 36. The measurements were carried out in a vacuum probe station with a pressure below 5×10^{-6} mbar (TTPX, Lakeshore). The transfer characteristics of GFET devices were measured using a dual-channel source meter (Keithley 2634B). One source measure unit (SMU) was programmed to regulate the gate voltage with respect to the drain, and another to maintain a constant drain voltage of 1 V. During the measurements, the source terminal was kept grounded.

2.12 Electrochemical characterization

The electrochemical characterization of RuSH CNM **8**-modified glassy carbon (GC) electrodes was performed using a CHI842B potentiostat (CH Instruments, Austin, TX, USA) in a three-electrode setup. The 3 mm glassy carbon electrode was used as working electrode *vs.* Ag wire reference electrode using the Fc/Fc^+ redox couple as the reference for the reported potentials. A coiled Pt wire was used as the counter electrode. The GC electrodes were pre-treated by cycling in 0.5 M H_2SO_4 in the potential window of −0.5 V to 0.5 V *vs.* Hg_2SO_4. All experiments were performed under argon atmosphere. The characterization of 1 mM RuSH **3** in 1 mM ferrocene/0.1 M $TBAPF_6$ in acetonitrile (ACN) was done using CV in the potential range from −2.0 V to 1.5 V *vs.* Ag (scan-rate: 100 mV s^{-1}). The solution was purged with argon for at least 15 minutes. To study the Ru species of RuSH CNMs at higher anodic potentials, the CNMs **8** were transferred onto the GC substrate (Fig. S49).[37] RuSH CNM **8**-modified GC electrodes were characterized in purged 0.1 M $TBAPF_6$/ACN by SWV (frequency = 15 Hz, amplitude = 25 mV, increment = 4 mV).

2.13 Luminescence quenching experiments

Luminescence quenching experiments were performed under Ar atmosphere in sealable screw-capped 1 cm cuvettes and in ACN using $[Ru(bpy)_3]Cl_2$ **17**, $[(dmbpy)_2Ru(phen(SBn)_2)](PF_6)_2$ **2**, $[(dmbpy)_2Ru(bpy)](PF_6)_2$ **19**, and $[(dmbpy)_2Ru(decbpy)](PF_6)_2$ **18** at a concentration of 10 μM. *N*-Methylphenothiazine (PTZ **16**) was added in small amounts using a 20 mM PTZ **16** solution in ACN. All sample preparation steps and titrations were performed in an argon-filled glovebox. Luminescence quenching data were recorded using two different excitation wavelengths, *i.e.*, at the maximum of the individual MLCT band as well as at 520 nm (operating wavelength of the GFET). For all complexes the two different excitation wavelengths resulted in the same Stern–Volmer quenching constants.

3. Results and discussion

3.1 Design and properties of the molecular precursors

First, the synthesis and properties of the molecular precursors **1**, **2** and **3** are discussed. The bottom-up design of the Ru(II) polypyridines is based on 5,6-bis(benzylthio)-1,10-phenanthroline ($phen(SBn)_2$ **13**) as the common head ligand. 5,6-Dibromo-1,10-phenanthroline **14** is obtained by a twofold bromination of 1,10-phenanthroline **15** followed by a nucleophilic aromatic substitution with *in situ* prepared sodium benzylthiolate yielding **13**.[29,30,38] Detailed experimental procedures as well as NMR and HRMS data are available in the SI section 1. The design of the head ligand is expected to have several advantages. The two neighboring sulfur atoms lead to an upright molecular orientation[39] as well as an increased stability of the SAM.[40] Aromatic thiols are also less affected by electron-beam irradiation then aliphatic groups[27,41] or carboxylic acids.[22,25] The loss of the head group as observed for the carboxylated Ru(II) complexes earlier[22] would severely impact a future bottom-side functionalization[42] of the nanosheet. In addition, variation of the substituents –H, $-CH_3$, –*t*Bu at the distal bipyridine ligands offers the possibility to investigate the effects of increasing steric demand and the possible changes of optical and electrochemical properties which might occur by introducing stronger sigma donor substituents.

Three different molecular precursors $[(bpy)_2Ru(phen(SBn)_2)](PF_6)_2$ **1**, $[(dmbpy)_2Ru(phen(SBn)_2)](PF_6)_2$ **2**, and $[(tbbpy)_2Ru(phen(SBn)_2)](PF_6)_2$ **3** were prepared by ligand exchange of **13** with $[(bpy)_2RuCl_2]$ **10**, $[(dmbpy)_2RuCl_2]$ **11** and $[(tbbpy)_2RuCl_2]$ **12**, respectively. The inherent Ru(II) polypyridine photoactivity and robustness[43,44] is found in the precursors **1**, **2** and **3**. Section 1 of the SI shows their normalized UV-Vis absorption and excitation spectra, as well as their emission spectra under argon and air atmosphere. These datasets indicate that the photophysical properties, in terms of light absorption are not affected by the substitution pattern at the two distal bipyridines, indicating relatively high electron density in the substituted phenanthroline ligand. The MLCT band maximum is in all cases at *ca.* 450 nm, while emission properties and photostability vary from bpy to dmbpy and tbbpy. The latter two behave identical due to their alkyl substituents. Compared to **2** and **3**, complex **1** exhibits a higher emission intensity with a blue-shifted emission maximum, as well as lower photostability in ACN which can be attributed to its larger excited state energy.

Self-assembly of **1**, **2** or **3** into RuSH SAMs **4**, **5** or **6** requires the removal of the benzyl protection groups with $AlCl_3$ in CH_2Cl_2 solution.[29] The aromatic dithiol complexes were not isolated due to their instability.[29] After filtration and CH_2Cl_2 removal, the deprotected ruthenium complexes were dissolved immediately in DMF. Au substrates were immersed into solutions of **1**, **2** or **3** to create RuSH SAMs **4**, **5** or **6**, respectively. The change of solvent to DMF was necessary as self-assembly from the CH_2Cl_2 solutions led to defective nanosheets. The compositions and properties of the SAMs and nanosheets are investigated in the following paragraphs starting with the methylated derivatives RuSH SAM **5** and RuSH CNM **8**. Note that for all studied samples no traces of aluminium or chlorine were detected by XPS.

3.2 Preservation of precursor properties upon self-assembly and nanosheet formation

In Fig. 2a, the X-ray photoelectron spectra of the Au surfaces after self-assembly show clearly the presence of the Ru(II)

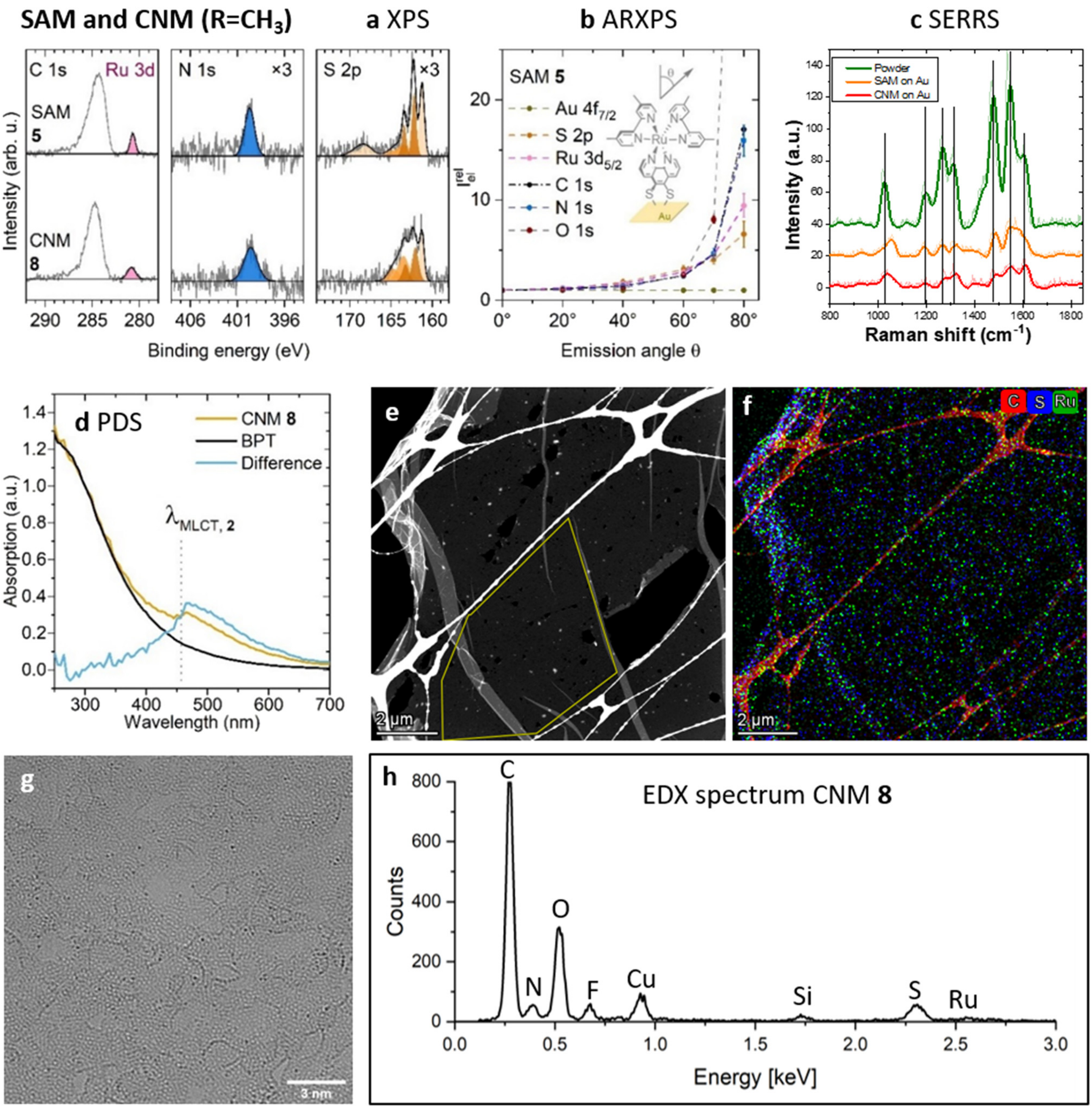

Fig. 2 (a) XP spectra of SAM **5** and CNM **8**. (b) ARXPS of SAM **5**, indicating that the S species in **5** are oriented towards the Au surface. (c) SERRS of SAM **5** and CNM **8**, confirming the fingerprint of precursor **2** in **5** and **8** and therefore a similar molecular structure. (d) PD spectra of CNM **8**. The absorption of CNM **8** is increased in the region of the MLCT transition compared to a non-functional BPT CNM. (e) HAADF STEM and (f and g) EDX mapping and -spectrum of CNM **8**. The white and red threads visible in (e) and (f), respectively, correspond to the structure of the lacey carbon used as substrate. EDX mapping show C, S and Ru are not accumulated in a single spot but are evenly distributed over the freestanding nanosheet. (h) HRTEM of CNM **8**, highlighting the presence of single heavy atoms in a matrix of lighter elements.

complex. The Ru $3d_{5/2}$ species at a binding energy (BE) of 280.7 eV (full-width at half maximum (fwhm) 0.6 eV) and the N 1s species related to polypyridines (399.7 eV, fwhm 1.2 eV) confirm the formation of a Ru(II) polypyridine containing layer.[22,45–48] The 0.8 nm thick layer shows a higher-than-expected overall carbon and sulfur content compared to the found Ru 3d amount as well as a variety of S 2p species.[23,27,49] The S 2p spectrum indicates the presence of sulfides (BE S $2p_{3/2,\ 1/2}$ = 161.2 and 162.4 eV, fwhm 0.7 eV), thiolates (BE S $2p_{3/2,\ 1/2}$ = 162.2 eV and 163.4 eV, fwhm 0.6 eV), thiols and/or disulfides (BE S $2p_{3/2,\ 1/2}$ = 163.5 and 164.7 eV, fwhm 2.0 eV), as well as oxidized sulfur species (BE S $2p_{3/2,\ 1/2}$ = 168.1 eV and 169.3 eV, fwhm 2.0 eV). The C 1s species peak maximum is found at 284.3 eV. No PF_6^-, Al^{3+} or Cl^- counterions were observed in the respective BE regions as seen in Fig. S44.

Fig. 2b shows the XP signals relative intensities recorded under variation of the photoelectron emission angle and normalized to the Au 4f signals intensity. The low increase in relative intensity for the S 2p species compared to Ru $3d_{5/2}$, C 1s, N 1s and O 1s indicates that the sulfur groups are close to the gold surface hinting on an upright orientation depicted schematically in Fig. 1. To verify further the anchoring of intact ruthenium dyes on the Au surface, SERRS measurements were performed (see Fig. 2c). Upon excitation at 488 nm, *i.e.* in resonance with the MLCT band of the RuSH complex (Fig. S35), Raman bands associated mainly with bipyridine (bpy) modes are found in the resonance Raman spectrum of the RuSH **2** powder at 1027, 1194, 1266, 1313, 1475, 1549 and 1606 cm^{-1} (vertical lines in Fig. 2c).[50,51] The bpy-associated bands are clearly detectable after immobilization of the Ru(II) complexes on Au in the SAMs SERRS spectrum, confirming the successful and stable immobilization. A uniform layer of material is also confirmed by the AFM images in Fig. S48. Mainly structures replicating the Au substrate are depicted with a RMS roughness of 0.9 nm as found before for SAMs prepared from solution.[31,45] The characteristics of the nanosheets formed by the subsequent low-energy electron irradiation are described in the following paragraph. XPS analysis shows the nanosheets thickness reduced to 0.6 nm. The broadening of the fwhm for Ru $3d_{5/2}$ and N 1s components by respectively 0.4 eV and 0.5 eV indicate the formation of new species and crosslinking as well.[21,22,52]

The S 2p doublet assigned to oxidized sulfur species at a BE of 168.1 eV (S $2p_{3/2}$) vanishes as well as the majority of the O 1s species (Fig. S44). Note, that the sample crosslinked in the external high vacuum system CNM **8a** in Fig. S45 did show a slightly increased CNM thickness of 0.8 nm as well as slightly different C 1s and O 1s signals.

AFM, Raman and adsorption data support the presence of intact complex cores after electron irradiation. The AFM image of nanosheet **8** on Au, shown in Fig. S48, appears very similar to the initial SAM's AFM image regarding roughness and topography. In Fig. 2c, the vibrations of the Ru(II) complex are still clearly detectable in the surface enhanced Raman spectrum of CNM **8**. The PDS spectrum in Fig. 2d confirms the Ru(II) ligand system is essentially intact and contributes to the absorptivity of the CNM even after its transfer from the growth Au substrate to quartz. As seen in the difference spectrum in blue, the RuSH CNM **8** (yellow) has an increased absorption in the region of the MLCT band of the parent molecule **2** when compared with a non-metal containing CNM prepared from BPT (Fig. 2d, black).[23]

CNM **8** forms a mm^2 sized, continuous and ultrathin film which can be transferred to different substrates like glassy carbon (Fig. S49) or TEM grids (Fig. 2e and f). The HAADF STEM investigation (Fig. 2e–h) shows for the first time the presence of Ru and S hetero atoms in the freestanding areas of CNM **8**. The recorded EDX mapping and the integrated EDX spectrum from the area marked by the yellow line (Fig. 2e) shows the heteroatoms do not accumulate on a single spot but are distributed throughout the entire carbon sheet. The HRTEM image of the freestanding film in Fig. 2h shows as well single, homogeneously distributed heavy atoms visible as darker spots, likely due to the darker contrast of Ru encapsulated by a lighter matrix. Ru atoms which remain isolated and not agglomerated confirm further that the molecular precursor could be successfully integrated into an ultrathin nanosheet. This further reinforces that Ru(II) polypyridine species can effectively withstand low-energy electron beam irradiation, making them ideal ready-to-use building blocks for nanosheets. In that way intrinsic photoactivity can be achieved without post-functionalization. The structurally similar complexes **1** and **3** are also able to form nanosheets as highlighted in the next paragraph.

3.3 Influence of the bipyridine ligands substitution pattern on the nanosheet formation

Fig. 3 summarizes SEM images, XPS, and PDS data of SAMs **4**, **6** and CNMs **7**, **9**. The XP spectra in Fig. 3a show no major differences between the SAMs **4**, **5**, **6**. Although the bipyridine ligands are substituted in the *para* position with –H in SAM **4** or –*t*Bu in SAM **6**, binding energy positions and intensities in all high-resolution spectra are comparable.

The respective Ru $3d_{5/2}$ and N 1s species typical for Ru(II) polypyridine are present as well as multiple S 2p species indicating various sulfur species including oxidized sulfur groups. Neither PF_6^- nor Cl^- counterions were found as shown in Fig. S47. This indicates that self-assembly does occur as expected and head ligand **13** is universally applicably to make custom building blocks for CNMs. The conversion into CNMs **7** and **9** is accompanied by similar spectral changes as for CNM **8**. The low-energy electron beam irradiation leads to a broadening of Ru $3d_{5/2}$ and N 1s peaks and reduction of peak intensities. Thicknesses reduce from 0.8 to 0.5 nm for the H substituted SAM-CNM conversion and from 0.9 to 0.5 nm for the *t*Bu substituted pair. The PDS investigation of the transferred nanosheets displayed in Fig. 3b shows again an increased absorption intensity in the visible range compared to non-functional BPT CNMs. The maxima of both CNM types are once more slightly higher than the absorption maxima of the parent complexes seen in UV-Vis spectra in Fig. S12 and S26. As argued before[22] and supported by the XPS peaks broadening, it is assumed that crosslinking causes an extension of

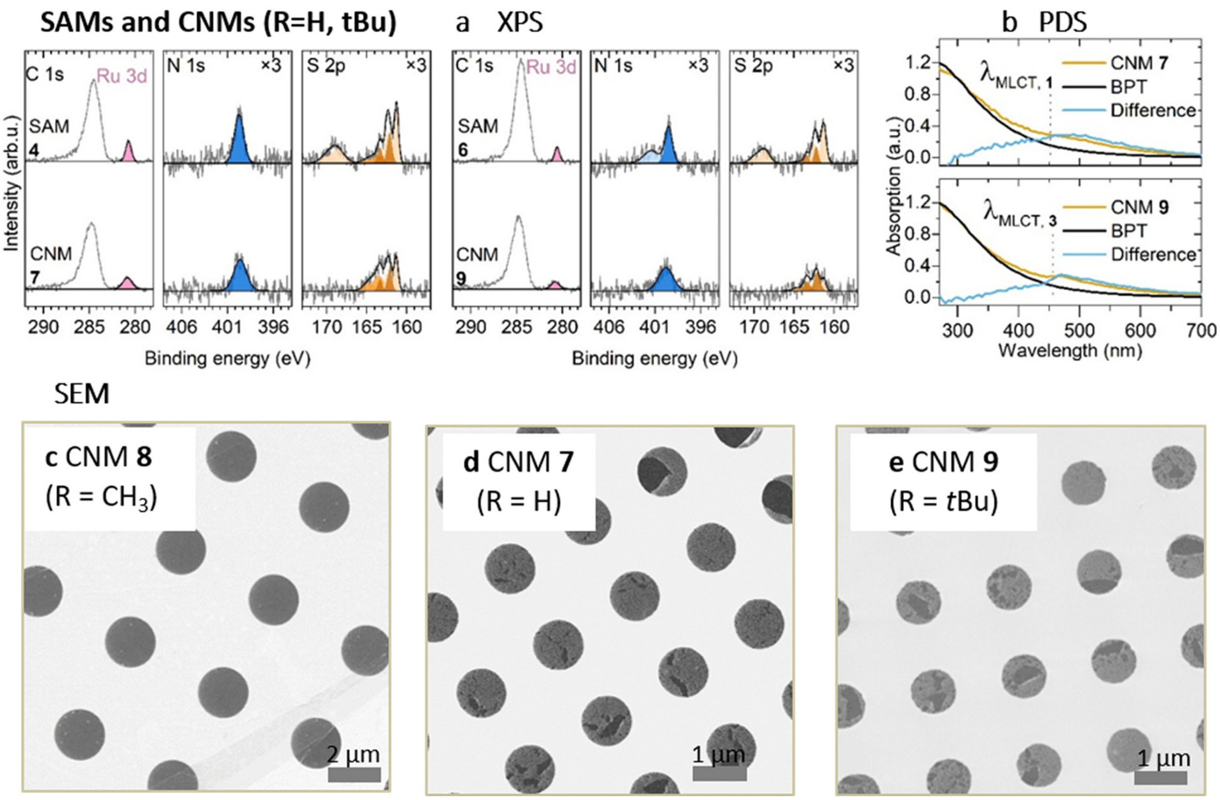

Fig. 3 The influence of the different terminal groups of precursors **1**, **2** and **3** on self-assembly and nanosheet formation is compared. (a) XPS data of the SAMs **4**, **6** and CNMs **7**, **9**. Both show similar compositions and changes due to the electron beam irradiation as SAM **5** and CNM **8** before. (b) PDS of CNMs **7** and **9**. Both show, similar to CNM **8**, an increase in visible light absorption compared to a non-functional BPT CNM. (c–e) SEM images of CNMs **7**–**9**. The SEM image of the CNM **8** highlights the formation of a freestanding film without defects on a support TEM grid. CNM **7** and **9** show freestanding but ruptured films indicating a lower mechanical stability.

the aromatic ligand system which reflects in a broad, slightly red shifted MLCT transition.

However, the type of substituent seems to be important for the stability of freestanding nanosheets as seen in Fig. 3c–e. Especially nanosheet **9**, which contains *t*Bu groups, showed a significantly weaker mechanical stability. Although covering the TEM grid fully, the nanosheets' freestanding areas without TEM grid support were found to be ruptured severely and easily damaged during the SEM investigation compared to nanosheet **8**. The steric demand of the *t*Bu group might hinder the dense packing of complexes in a monolayer, therefore yielding a more fragile nanosheet. The reason why the unsubstituted complex in CNM **7** did not perform similarly well as the methyl-substituted one is not clear. A possible explanation might be slightly lower thickness of the nanosheets of 0.5 nm. As seen in Fig. S50, ruptured CNMs with a thickness of 0.5 nm can be formed similarly from the methylated complex **2** if immersion times for self-assembly were drastically shortened to 24 h. In general, freestanding nanosheets for such complexes seem to be only obtainable with a layer thickness of above 0.5 nm. As complex **2** did result reproducibly in mechanical stable nanosheets, all further investigations were carried out with nanosheet **8**. Next, the functional properties of nanosheet **8** are investigated in detail.

3.4 Electrochemical activity and optoelectrical behavior of the nanosheets

For the first time, we can report on the electrochemical activity of a carbon nanomembrane made by low-energy electron irradiation of a single layer of transition metal complexes as seen in the SWV graphs in Fig. 4. Electrochemical characterizations by CV and SWV were either recorded with RuSH CNM **8** modified GC substrates as working electrodes or of the deprotected RuSH **3** dissolved in ACN. All potentials are reported *versus* the Fc/Fc$^+$ redox couple. Fig. 4a shows the reference CV of a 1 mM solution of **3** in 1 mM ferrocene/0.1 M TBAPF$_6$ in ACN. Deprotected complex **3** was used as reference instead of complex **2** as the *t*Bu groups are expected to improve solubility in ACN compared to Me groups, at the same time not influencing the electrochemistry of the complex (for CV of protected complex **3**, see Fig. S51).[53] Reduction peaks are visible in the potential range from −2.25 V (**1**) to −1.8 V, which are related to the reduction of 4,4′-di-*tert*-butyl-2,2′-bipyridine (tbbpy).[54] The peaks at −1.45 V (**2**) and −1.31 V (**3**) are ascribed to the reduction of the phenanthroline dithiolate moiety.[54,55] The reduction peaks at −0.96 V and −0.5 V could not be clearly assigned but might result from Ru species that underwent structural changes under oxidative conditions such as thiol

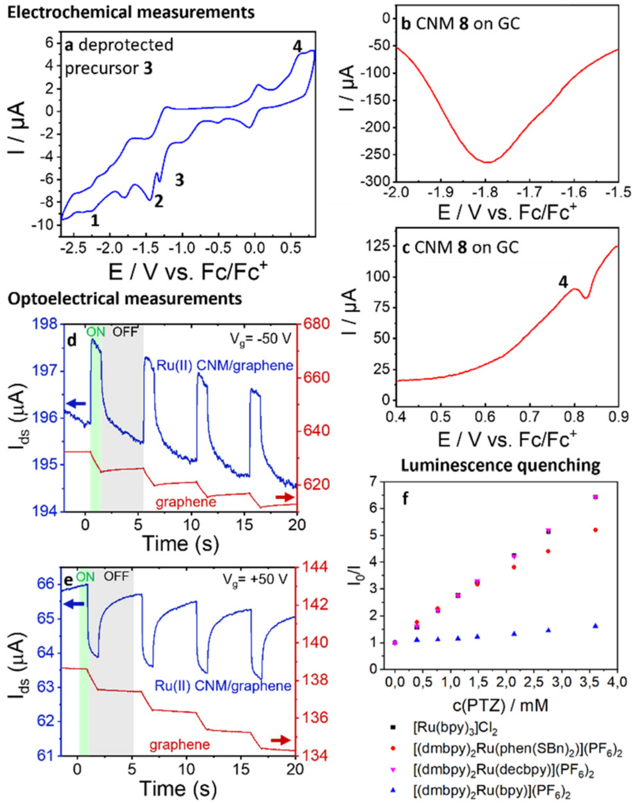

Fig. 4 Electrochemical and optoelectrical properties of CNM **8**. (a) The CV of the deprotected precursor **3** shows several reduction peaks related to the polypyridine ligands (**1–3**) as well as the redox peaks for Ru (**4**) (electrode area: 28.26 mm^2). (b and c) In the SWV of CNM **8** modified GC, a redox peak for Ru can be identified but no distinct peaks for the ligands are visible (electrode area: 38.48 mm^2). (d and e) The photoactivity of CNM **8** is shown by recording the photo-current response I_{ds} of a RuSH CNM/GFET device in blue upon ON/OFF switching of a 520 nm laser at a gate voltage of (d) V_g = −50 V and (e) V_g = 50 V. The current response I_{ds} of a bare GFET reference device under identical illumination conditions (red) shows a different behavior demonstrating the CNMs' photoactivity. The photoactivity performance of CNMs seems to correlate with the (f) luminescence quenching behavior of the molecular building blocks with PTZ **16**, as [(dmbpy)$_2$Ru(phen(SBn)$_2$)](PF$_6$)$_2$ **2**, [Ru(bpy)$_3$]Cl$_2$ **17** [(dmbpy)$_2$Ru(decbpy)](PF$_6$)$_2$ **18** show a higher reactivity with **16** than [(dmbpy)$_2$Ru(bpy)](PF$_6$)$_2$ **19**.

couplings. An irreversible oxidation of the dithiolate and Ru metal center (**4**) is observed at 0.40 V and 0.66 V, respectively.[28] The SWV studies in Fig. 4b and c of RuSH CNM **8** transferred from the growth substrate to glassy carbon show, that separated characteristic reduction peaks of the ligands (*e.g.* (**1**), (**2**) and (**3**)) are not clearly detectable, probably due to the cross-linking. However, SWV does display the redox active Ru peak at 0.8 V *vs.* Fc/Fc$^+$ (**4**) at the cross-linked CNM **8**, which is in very good agreement with the CV studies of the protected Ru(II) complex, revealing a reversible Ru(II)/Ru(III) species at 0.78 V *vs.* Fc/Fc$^+$ as displayed in Fig. S51. The mass fraction of Ru was determined by deconvolution of the SWV results with a full-width Lorentzian curve at half-maximum at 0.8 V *vs.* Fc/Fc$^+$. Based on the SWV peak area, the charge was determined by using Faraday's Law for a 1-electron redox process, taking the electrode area into account. The values determined for two different batches were 55.8 pmol mm^{-2} and 61.7 pmol mm^{-2}, respectively. The repeatability of the SWV experiments suggests that the 2D material is strongly bound to the electrode surface, despite adhesion occurring solely through van der Waals forces. This opens up the possibility to use this material also for post-functionalization of electrode surfaces due to their electrochemical response and stability, whereas SAMs do require a match between the headgroup and the electrode material limiting therefore their applicability.

In addition, upon illumination with visible light a single layered CNM **8** shows also an optoelectrical response when placed on GFETs. The photo-activity of RuSH CNM **8** can be studied by assembling a van der Waals heterostructure with the graphene channel and characterizing the optoelectrical response of the respective device upon illumination with a 520 nm laser. In total 15 GFET devices are available on the GFET chip as seen in Fig. S52. While transferring CNM onto eleven GFET devices, the bottom four devices were intentionally left uncovered representing bare graphene GFETs. This arrangement on the same chip allowed for the direct photo-activity comparison of RuSH CNM/graphene and graphene. The CNM on top of the graphene channel results in a shift of the Dirac point voltage (V_D) in the graphene by ∼6 V to lower values reflecting the induced n-type doping (see Fig. S53a). The photo-response curves of both device types upon periodic irradiation (89.6 mW cm^{-2}, V_{ds} = 1 V) at the gate voltages, V_g of −50 V and 50 V, are shown in Fig. 4d and e, respectively. The Ru(II) CNM/graphene device generates a positive photo-current at the hole conduction regime (V_g = −50 V) and a negative photo-current at electron conduction regime (V_g = 50 V). In contrast, the bare graphene device exhibits only a photo-gating response, attributed to the interaction between graphene and SiO$_2$, particularly at a high laser power intensity of 89.6 mW cm^{-2}. The results are consistent with the observed up-shifting of V_D by increasing the laser intensity displayed in Fig. S53b, indicating an increase of p-type doping under irradiation. The observed photo-current behavior might be described by an electron transfer from the underlying graphene to the Ru(II) complex in the excited state due to illumination, thus enhancing p-type behavior of the graphene. Upon MLCT excitation of the RuSH CNM (HOMO ≈ −5.4 eV, MLCT excited state ≈ −2.7 eV), a photogenerated hole is created in the CNM HOMO. Given the graphene Fermi level (EF ≈ −4.5 eV), electron transfer from graphene to the CNM is energetically favorable (downhill by ∼0.9 eV). This process removes electrons from graphene, increasing p-type doping, and yields the observed Dirac point shift and the photocurrent polarity. Also, a possible photogating of the graphene can occur due to the charge separation within the CNM upon the MLCT in the observed photocurrent. The small baseline drift of the real-time current measurements in both Ru-CNM/graphene and bare graphene devices is attributed to charge trapping/de-trapping at the graphene-dielectric interface.

In our previous work,[22] we showed that generating a stable photo-current in Ru(II) CNMs made from the carboxylic acid precursor $[(dmbpy)_2Ru(decbpy)](PF_6)_2$ required a much larger amount of photo-active material, meaning a multilayered material with a thickness of ∼3 nm. With the monolayered Ru(II) CNM having a thickness <1 nm, we previously noted a rapid decay in the photo-current due to interference from negative photo-current caused by photogating effects. This issue of photo-current instability in the monolayer form is now effectively mitigated by the presence of sulfur in the RuSH CNM structure. A possible explanation for the superior performance of the RuSH CNM monolayer to the Ru(II) CNM monolayer used previously, might be deducted from the photochemical behavior of the molecular units likely present in the 2D material. Fig. 4f shows the luminescence quenching of differently substituted Ru(II) polypyridine molecules in the presence of the electron donor PTZ **16** in ACN solution under Ar atmosphere. $[Ru(bpy)_3]Cl_2$ **17** serves as a reference. The molecular precursor **2** for RuSH CNM **8** and $[(dmbpy)_2Ru(decbpy)](PF_6)_2$ **18** for the previous Ru(II) CNM[22] were compared. $[(dmbpy)_2Ru(bpy)](PF_6)_2$ **19** is taken into account as well, as carboxylic acid groups are cleaving quickly under the electron beam.[22,25] Fig. 4f shows the likeliness of electron transfer from PTZ to the Ru(II) complexes. The complexes luminescence quenching depends strongly on the substituents of the bipyridine ligands as the substituents sterical demand and electronic properties affect the position of the Ru(II/III) redox potential.[50,56,57] The luminescence quenching constant K_{SV} is highest for ref. 17 (K_{SV} = 1.51 × 10^3 l mol^{-1}) and precursor **18** (K_{SV} = 1.52 × 10^3 l mol^{-1}) followed by precursor **2** (K_{SV} = 1.26 × 10^3 l mol^{-1}) and lowest for **19** (K_{SV} = 1.61 × 10^2 l mol^{-1}). Although the electron withdrawing effect of the carboxylic group of **18** is very beneficial for the electron transfer, the luminescence quenching is low if the carboxylic group is missing as seen on **19**. As carboxylic acid groups are largely lost under the electron beam,[22,25] **19** and not **18** is assumed to be the main representative in the Ru(II) CNMs showing previously a weak optoelectrical response.[22] We therefore assume that the RuSH CNMs' superior monolayer behavior is indeed due to the preservation of most of the thiol groups during electron irradiation. This means that the 2D materials photochemical behavior can be directly influenced by the molecular structure in the nanomaterial. This indicates not only a rule of design for the photochemically active 2D material but also hints on the possibility to examine the behavior of the final 2D sheet before with single molecules luminescence quenching experiments. In that way, the intentional selection and synthesis of precursors allows to tailor the nanosheets properties to the desired application.

4. Conclusion

This study demonstrates the modular preparation of novel 2D materials by self-assembling thiolated Ru(II) polypyridine complexes onto gold (Au) surfaces, followed by electron beam-induced crosslinking into nanosheets. The complexes containing different bipyridine ligands offer flexibility for introducing different substituents on demand. For instance, the dithiol group on the head ligand enables reliable self-assembly *via* Au-thiolate bonds, while substituents like –H, $-CH_3$, or –*t*Bu on the distal bipyridines are used to vary the steric demand whilst keeping the molecules photophysical properties similar. Spectroscopic, electrochemical and microscopic analysis confirms that both the Ru(II) core and the thiol group remain intact during electron beam irradiation and substrate removal offering the possibility for post-functionalization with *e.g.* hydrogen evolution catalysts.

By altering the distal bipyridine ligands, nanosheets with similar elemental composition and absorption properties were obtained, although their mechanical stability varied. Specifically, freestanding nanosheets with –H and –*t*Bu substituents were slightly less stable, probably due to their thickness of only 0.5 nm and the hindered self-assembly caused by the bulky *t*Bu group. Electrochemical and optoelectrical tests revealed that the Ru(II) centers remain active, even when embedded in the ultrathin nanosheets, which function as the active layer on the electrode or field-effect transistor used. Additionally, the presence of thiol substituents on the precursor enhanced the activity, as indicated also in luminescence quenching experiments with model substances. With a thickness of less than 1 nm, these nanosheets exhibit unique structural and photoactive properties, making them ideal candidates for applications in catalysis, sensing, and device miniaturization.

Author contributions

M. K. and A. T. have designed the research with contributions of B. D.-I., C. K. and S. R. M. K. performed XPS characterization, optical microscopy and AFM. M. K., V. M. and R. G. performed sample preparation. E. N. and H. R. R. performed and evaluated optoelectrical measurements. C. N. performed SEM characterization. T. W. microfabricated GFETs. R. L., J. B., and U. K. performed and analyzed STEM-EDX and HRTEM experiments and contributed to the manuscript. F. H.-W., L. S. D. and B. D.-I. performed and evaluated SERRS and PDS data. M. P. designed the PDS setup. A. M. and K. W. both synthesized $phen(SBn)_2$ and complexes **1**, **2** and **3**. A. M. additionally synthesized 5,6-dibromo-1,10-phenanthroline, $[(dmbpy)_2Ru(bpy)](PF_6)_2$ and $[(dmbpy)_2Ru(decbpy)](PF_6)_2$. A. M. performed all NMR, ground-state UV-Vis, emission and mass spectrometric analyses and characterizations, interpreted the data and prepared graphics. A. M. performed luminescence quenching experiments. J. K. performed the electrochemical characterization experiments and the quantification of the Ru content. M. K., D. H. and A. T. wrote the manuscript with contributions of all co-authors.

Conflicts of interest

There are no conflicts to declare.

Data availability

The data related to this study are included in the main text or supplementary information (SI). Supplementary information is available, which includes detailed information on the synthesis and characterization of all Ru(II) complexes and their precursor molecules (Section 1) including 1H-, 13C-NMR-, H-H-COSY-, (simulated) MS-, UV-Vis absorption, emission and emission excitation spectra, detailed information on the preparation of SAMs and CNMs (Section 2), including additional XPS data, AFM, SEM and OM images, and details on the electrochemical characterization and optoelectrical measurements of nanosheet 8 (Section 3) including SWVs and charge transfer curves. See DOI: **https://doi.org/10.1039/d5nr02717a**.

Any additional data are available from the corresponding author on a reasonable request.

Acknowledgements

The authors thank the DFG for financial support within the SFB-TRR 234 "CataLight" projects C1, C4, B2, B7 and Z2. The authors acknowledge Stephanie Höppener and Ulrich S. Schubert for providing access to the SEM. The SEM facilities of the Jena Center for Soft Matter (JCSM) were established with a grant from the DFG.

References

1 D. Kim, K. K. Sakimoto, D. Hong and P. Yang, *Angew. Chem., Int. Ed.*, 2015, **54**, 3259–3266.
2 V. Vogl, M. Åhman and L. J. Nilsson, *J. Cleaner Prod.*, 2018, **203**, 736–745.
3 K. Kolbe, *Transp. Policy*, 2019, **80**, 1–11.
4 F. Kurnia, J. A. Scott, N. Valanoor and J. N. Hart, *J. Mater. Chem. C*, 2023, **11**, 802–826.
5 B. Zhang and L. Sun, *Chem. Soc. Rev.*, 2019, **48**, 2216–2264.
6 D. Deng, K. S. Novoselov, Q. Fu, N. Zheng, Z. Tian and X. Bao, *Nat. Nanotechnol.*, 2016, **11**, 218–230.
7 B. Luo, G. Liu and L. Wang, *Nanoscale*, 2016, **8**, 6904–6920.
8 G. G. Shanker, A. Biswas and S. Ogale, *J. Phys. Energy*, 2021, **3**, 022003.
9 C. Backes, *et al.*, *2D Mater.*, 2020, **7**, 022001.
10 X. Liu, E. K. Lee and J. H. Oh, *Small*, 2014, **10**, 3700–3706.
11 P. Kumar, R. Boukherroub and K. J. Shankar, *Mater. Chem. A*, 2018, **6**, 12876–12931.
12 F. Frehill, J. G. Vos, S. Benrezzak, A. A. Koós, Z. Kónya, M. G. Rüther, W. J. Blau, A. Fonseca, J. B. Nagy, L. P. Biró, A. I. Minett and M. i. h. Panhuis, *J. Am. Chem. Soc.*, 2002, **124**, 13694–13695.
13 D. L. Ashford, M. K. Gish, A. K. Vannucci, M. K. Brennaman, J. L. Templeton, J. M. Papanikolas and T. J. Meyer, *Chem. Rev.*, 2015, **115**, 13006–13049.
14 D. Cedeno, A. Krawicz, P. Doak, M. Yu, J. B. Neaton and G. F. Moore, *J. Phys. Chem. Lett.*, 2014, **5**, 3222–3226.
15 S. Troppmann, E. Brandes, H. Motschmann, F. Li, M. Wang, L. Sun and B. König, *Eur. J. Inorg. Chem.*, 2016, **2016**, 554–560.
16 A. Turchanin, *Chimia*, 2019, **73**, 473–479.
17 A. Turchanin and A. Gölzhäuser, *Adv. Mater.*, 2016, **28**, 6263–6263.
18 A. Turchanin and A. Gölzhäuser, *Prog. Surf. Sci.*, 2012, **87**, 108–162.
19 X. Zhang, C. Neumann, P. Angelova, A. Beyer and A. Gölzhäuser, *Langmuir*, 2014, **30**, 8221–8227.
20 P. Angelova, H. Vieker, N.-E. Weber, D. Matei, O. Reimer, I. Meier, S. Kurasch, J. Biskupek, D. Lorbach, K. Wunderlich, L. Cheng, A. Terfort, M. Klapper, K. Müllen, U. Kaiser, A. Gölzhäuser and A. Turchanin, *ACS Nano*, 2013, **7**, 6489–6497.
21 Z. Tang, E. Chulanova, M. Küllmer, A. Winter, J. Picker, C. Neumann, K. Schreyer, F. Herrmann-Westendorf, A. Arnlind, B. Dietzek, U. S. Schubert and A. Turchanin, *Nanoscale*, 2021, **13**, 20583–20591.
22 M. Küllmer, F. Herrmann-Westendorf, P. Endres, S. Götz, H. R. Rasouli, E. Najafidehaghani, C. Neumann, R. Gläßner, D. Kaiser, T. Weimann, A. Winter, U. S. Schubert, B. Dietzek and A. Turchanin, *Angew. Chem., Int. Ed.*, 2022, **61**, e202204953.
23 A. Turchanin, D. Käfer, M. El-Desawy, C. Wöll, G. Witte and A. Gölzhäuser, *Langmuir*, 2009, **25**, 7342–7352.
24 C. Neumann, R. A. Wilhelm, M. Küllmer and A. Turchanin, *Faraday Discuss.*, 2021, **227**, 61–79.
25 C. Neumann, M. Szwed, M. Frey, Z. Tang, K. Koziel, P. Cyganik and A. Turchanin, *ACS Appl. Mater. Interfaces*, 2019, **11**, 31176–31181.
26 M. Zharnikov, S. Frey, K. Heister and M. Grunze, *Langmuir*, 2000, **16**, 2697–2705.
27 M. Zharnikov, W. Geyer, A. Gölzhäuser, S. Frey and M. Grunze, *Phys. Chem. Chem. Phys.*, 1999, **1**, 3163–3171.
28 D. Schallenberg, A. Neubauer, E. Erdmann, M. Tänzler, A. Villinger, S. Lochbrunner and W. W. Seidel, *Inorg. Chem.*, 2014, **53**, 8859–8873.
29 L. K. Keniley Jr., L. Ray, K. Kovnir, L. A. Dellinger, J. M. Hoyt and M. Shatruk, *Inorg. Chem.*, 2010, **49**, 1307–1309.
30 S. Rau, B. Schäfer, A. Grüßing, S. Schebesta, K. Lamm, J. Vieth, H. Görls, D. Walther, M. Rudolph, U. W. Grummt and E. Birkner, *Inorg. Chim. Acta*, 2004, **357**, 4496–4503.
31 Z. Tang, C. Neumann, A. Winter and A. Turchanin, *Nanoscale*, 2020, **12**, 8656–8663.
32 C. T. Nottbohm, A. Turchanin, A. Beyer, R. Stosch and A. Gölzhäuser, *Small*, 2011, **7**, 874–883.
33 N. Leopold and B. Lendl, *J. Phsy. Chem. B*, 2003, **24**, 5723–5727.
34 M. L. Hupfer, F. Herrmann-Westendorf, M. Kaufmann, D. Weiß, R. Beckert, B. Dietzek and M. Presselt, *Chem. – Eur. J.*, 2019, **25**, 8630–8634.
35 M. L. Hupfer, F. Herrmann-Westendorf, B. Dietzek and M. Presselt, *Analyst*, 2021, **146**, 5033–5036.

36 D. Kaiser, Z. Tang, C. Neumann, A. Winter, R. Kahle, L. Georgi, T. Weimann, M. Siegmann, S. Gräfe, A. Centeno, A. Zurutuza and A. Turchanin, *Appl. Phys. Rev.*, 2021, **8**, 031410.

37 N. Elgrishi, K. J. Rountree, B. D. McCarthy, E. S. Rountree, T. T. Eisenhart and J. L. Dempsey, *J. Chem. Educ.*, 2018, **95**, 197–206.

38 A. Stumper, T. D. Pilz, M. Schaub, H. Görls, D. Sorsche, K. Peuntinger, D. Guldi and S. Rau, *Eur. J. Inorg. Chem.*, 2017, **2017**, 3799–3810.

39 J. C. Love, L. A. Estroff, J. K. Kriebel, R. G. Nuzzo and G. M. Whitesides, *Chem. Rev.*, 2005, **105**, 1103–1170.

40 Y.-S. Shon and T. R. Lee, *J. Phys. Chem. B*, 2000, **104**, 8192–8200.

41 S. A. M. Osborne and Z. Pikramenou, *Faraday Discuss.*, 2015, **185**, 219–231.

42 Z. Zheng, C. T. Nottbohm, A. Turchanin, H. Muzik, A. Beyer, M. Heilemann, M. Sauer and A. Gölzhäuser, *Angew. Chem., Int. Ed.*, 2010, **49**, 8493–8497.

43 Y.-J. Yuan, Z.-T. Yu, D.-Q. Chen and Z.-G. Zou, *Chem. Soc. Rev.*, 2017, **46**, 603–631.

44 A. Juris, V. Balzani, F. Barigelletti, S. Campagna, P. Belser and A. von Zelewsky, *Coord. Chem. Rev.*, 1988, **84**, 85–277.

45 M. Küllmer, P. Endres, S. Götz, A. Winter, U. S. Schubert and A. Turchanin, *ACS Appl. Mater. Interfaces*, 2021, **13**, 60544–60552.

46 H. Rensmo, K. Westermark, S. Södergren, O. Kohle, P. Persson, S. Lunell and H. Siegbahn, *J. Chem. Phys.*, 1999, **111**, 2744–2750.

47 L. C. Mayor, J. Ben Taylor, G. Magnano, A. Rienzo, C. J. Satterley, J. N. O'Shea and J. Schnadt, *J. Chem. Phys.*, 2008, **129**, 114701.

48 L. C. Mayor, A. Saywell, G. Magnano, C. J. Satterley, J. Schnadt and J. N. O'Shea, *J. Chem. Phys.*, 2009, **130**, 164704.

49 Y. Zubavichus, M. Zharnikov, Y. Yang, O. Fuchs, E. Umbach, C. Heske, A. Ulman and M. Grunze, *Langmuir*, 2004, **20**, 11022–11029.

50 P. A. Mabrouk and M. S. Wrighton, *Inorg. Chem.*, 1986, **25**, 526–531.

51 S. Tschierlei, B. Dietzek, M. Karnahl, S. Rau, F. M. MacDonnell, M. Schmitt and J. Popp, *J. Raman Spectrosc.*, 2008, **39**, 557–559.

52 C. Neumann, D. Kaiser, M. J. Mohn, M. Füser, N.-E. Weber, O. Reimer, A. Gölzhäuser, T. Weimann, A. Terfort, U. Kaiser and A. Turchanin, *ACS Nano*, 2019, **13**, 7310–7322.

53 D. van der Westhuizen, J. Conradie and K. G. von Eschwege, *Electroanalysis*, 2020, **32**, 2838–2851.

54 A. K. Mengele, C. Müller, D. Nauroozi, S. Kupfer, B. Dietzek and S. Rau, *Inorg. Chem.*, 2020, **59**, 12097–12110.

55 E. Erdmann, M. Lütgens, S. Lochbrunner and W. W. Seidel, *Inorg. Chem.*, 2018, **57**, 4849–4863.

56 T. Rajendran, P. Thanasekaran, S. Rajagopal, G. A. Gnanaraj, C. Srinivasan, P. Ramamurthy, B. Venkatachalapathy, B. Manimaran and K.-L. Lu, *Phys. Chem. Chem. Phys.*, 2001, **3**, 2063–2069.

57 H. Shalan, A. Colbert, T. T. Nguyen, M. Kato and L. Cheruzel, *Inorg. Chem.*, 2017, **56**, 6558–6564.